NIH Public Access
Author Manuscript
Phys Med Biol. Author manuscript; available in PMC 2015 January 20.

Published in final edited form as:
Phys Med Biol. 2014 January 20; 59(2): 465–484. doi:10.1088/0031-9155/59/2/465.

Binding Dynamics of Targeted Microbubbles in Response to Modulated Acoustic Radiation Force

Shiying Wang[1], **John A Hossack**[1], **Alexander L Klibanov**[1,2], and **F William Mauldin Jr**[1,3]

[1]Department of Biomedical Engineering, University of Virginia, Charlottesville, VA 22908, USA

[2]Division of Cardiovascular Medicine, University of Virginia, Charlottesville, VA 22908, USA

Abstract

Detection of molecular targeted microbubbles plays a foundational role in ultrasound-based molecular imaging and targeted gene or drug delivery. In this paper, an empirical model describing the binding dynamics of targeted microbubbles in response to modulated acoustic radiation forces in large vessels is presented and experimentally verified using tissue-mimicking flow phantoms. Higher flow velocity and microbubble concentration led to faster detaching rates for specifically bound microbubbles ($p < 0.001$). Higher time-averaged acoustic radiation force intensity led to faster attaching rates and a higher saturation level of specifically bound microbubbles ($p < 0.05$). The level of residual microbubble signal in targeted experiments after cessation of radiation forces was the only response parameter that was reliably different between targeted and control experiments ($p < 0.05$). A related parameter, the ratio of residual-to-saturated microbubble signal (R_{resid}), is proposed as a measurement that is independent of absolute acoustic signal magnitude and therefore able to reliably detect targeted adhesion independently of control measurements ($p < 0.01$). These findings suggest the possibility of enhanced detection of specifically bound microbubbles in real-time, using relatively short imaging protocols (approximately 3 min), without waiting for free microbubble clearance.

1. Introduction

Microbubbles – comprising low solubility gas bubbles (less than 10 μm in diameter) stabilized with a shell (lipid, protein, or polymer) – are the most popular ultrasound contrast agent (De Jong *et al* 1992, Klibanov 2002, Lindner 2004a). Targeted microbubbles are fabricated by incorporating microbubble shell with ligands to specific molecular markers (*e.g.* ICAM-1 and P-selectin for cardiovascular-related diseases) (Klibanov *et al* 1997, Unnikrishnan and Klibanov 2012). These ligands allow microbubbles to attach to specific regions of the vascular endothelium through the specific ligand-receptor bond, thereby enabling applications for both targeted molecular imaging (Dayton and Ferrara 2002, Lindner 2004b, Klibanov 2007, Deshpande *et al* 2010) and targeted gene/drug delivery (Ferrara *et al* 2007, Mayer and Bekeredjian 2008, Hernot and Klibanov 2008). In order to increase the binding efficacy of targeted microbubbles to potential binding sites, especially in large blood vessel environments, acoustic radiation force (ARF) is frequently applied

[3]To whom any correspondence should be addressed.

NIH-PA Author Manuscript
NIH-PA Author Manuscript
NIH-PA Author Manuscript

NIH-PA Author Manuscript

NIH-PA Author Manuscript

NIH-PA Author Manuscript

(Dayton *et al* 1999, Zhao *et al* 2004, Rychak *et al* 2007, Gessner *et al* 2012). In addition, targeted microbubbles incorporated with multiple ligands can be used to further increase adhesion to the vessel wall (Ferrante *et al* 2009).

The detection and enhancement of signals derived from ligand-receptor bound microbubbles ("specifically bound adherent microbubbles") and suppression of surrounding tissue and freely circulating microbubbles is a central technical challenge in ultrasound-based targeted molecular imaging. Nonlinear signal detection methods (*e.g.* pulse inversion or harmonic imaging) are frequently used to eliminate signals from surrounding tissue (Phillips 2001, Phillips and Gardner 2004, Deshpande *et al* 2010). Thereafter, signals from "free" microbubbles are suppressed by lengthy waiting periods (*e.g.* 15 – 30 min) to clear the vessel lumen (Lindner *et al* 2001, Pochon *et al* 2010), or by low-pass interframe filtering from recently developed real-time targeted molecular imaging techniques (Needles *et al* 2009, Hu *et al* 2010, Patil *et al* 2011). Several related fast-imaging methods have demonstrated efficacy in small blood vessel environments, such as in small blood vessel environments suitable for cancer applications (Pysz *et al* 2012b, Hu *et al* 2013, Pysz *et al* 2012a). In addition, a new technique called singular spectrum-based targeted molecular imaging (SiSTM) is able to isolate signals from adherent microbubbles by analyzing the statistical properties of different signal sources (Mauldin *et al* 2012, Wang *et al* 2013). However, these approaches are only capable of detecting adherent microbubbles and cannot distinguish between non-specific molecular binding (undesirable "signal"), which increases with applied ARF, and specific binding (desirable "signal"). Therefore, all of these techniques require control groups to estimate the non-specific adhesion "background" signal. Presence of the targeted molecular along the vascular wall is assumed if there is a significant increase in adherent microbubbles between control and targeted groups (Stieger *et al* 2008, Nitta-Seko *et al* 2010, Masseau *et al* 2012, Pysz *et al* 2012b). A consequence is that multiple microbubble populations may be used resulting in very long procedure times, up to 30–40 minutes (Lindner *et al* 2000, Pysz *et al* 2012b), as it often requires at least 20 minutes for microbubbles to clear the vasculature after a single injection (Lindner *et al* 2000, Pysz *et al* 2012b, Masseau *et al* 2012). In addition, the specificity of the detection of molecular targets can be limited due to detection of undesired positive signal from control groups (the control group microbubble signal is often 20 % or more of targeted group signal) (Masseau *et al* 2012, Pysz *et al* 2012b).

In this paper, we hypothesize that measurements of microbubble binding dynamics under modulated ARF can provide enhanced detection of targeted microbubble adhesion from non-specific binding in large blood vessel environments. A model for microbubble dynamics in response to modulated ARF is proposed and the model is compared to experimental observation in control and targeted flow phantom experiments. The relationship between experimental conditions and model parameters are determined for varied flow velocities, microbubble concentrations, and time averaged ARF intensity. Parameters uniquely obtainable from microbubble response to modulated radiation force are assessed for detection of targeted adhesion independent of control populations.

NIH-PA Author Manuscript

NIH-PA Author Manuscript

NIH-PA Author Manuscript

1.1. Theory

Suitable models that can predict microbubble binding dynamics in response to modulated ARF are important for enhanced detection of specifically, versus non-specifically, bound adherent microbubbles as they can guide selection of parameter extraction for optimal detection sensitivity and specificity. A previous study by Bell provided a theoretical model for cell-to-cell adhesion when the adhesion is mediated by reversible specific bonds attached on a cell membrane (Bell 1978). The kinetic equation can be written as:

$$\frac{\mathrm{d}N_{\mathrm{b}}}{\mathrm{d}t}=k_{+}N_{1\mathrm{f}}N_{2\mathrm{f}}-k_{-}N_{\mathrm{b}} \quad (1)$$

where N_{b} is the number of bound receptors per unit area which serve to bridge the cells; $N_{1\mathrm{f}}$ and $N_{2\mathrm{f}}$ are corresponding numbers of unbound receptors from two cells; k_{+} and k_{-} are reaction rate constants for association and disassociation processes, respectively. Based on this model, Hammer and co-workers developed dynamic models for receptor-mediated adhesion of cells under a shear field of fluid within a surface coated fluid channel by analyzing the force balance of an individual cell attached to a channel wall (Hammer and Lauffenburger 1989, Chang and Hammer 2000, Bhatia *et al* 2003, Krasik *et al* 2006). Thereafter, Maul and co-authors implemented the computational model on both single-and dual-targeted microbubbles to improve selection of ligands and binding strength (Maul *et al* 2010). However, the computational models for adhesive dynamics of targeted microbubbles were based on single microbubble analysis. In addition, the effects of ARF were not considered.

Unlike micro analysis of single microbubbles, Klibanov and co-authors developed a model for the macro analysis of targeted liposomes through experiments in multiwall plates (Klibanov *et al* 1985). Time courses of bound liposome concentration and dissociation constants were obtained. Based on this study, Klibanov and co-authors studied the binding and detachment dynamics of microbubbles targeted to P-selectin in a parallel-plate flow chamber (Takalkar *et al* 2004). Influence of flow shear stress and surface density of targeted receptor on binding and detachment dynamics were investigated. However, the effects of ARF on microbubble binding dynamics were not included.

In order to model the binding dynamics of targeted microbubbles in response to modulated ARF, the kinetic equation of adherent microbubbles on the bottom surface of the vessel is described in an analogous manner to (1):

$$\frac{\mathrm{d}N_{\mathrm{AMB}}}{\mathrm{d}t}=k_{+}(N_{\mathrm{FMB}}d)N_{\mathrm{B}}-k_{-}N_{\mathrm{AMB}} \quad (2)$$

where N_{AMB} is the number of adherent microbubbles per unit area on the surface of bottom wall; N_{FMB} is the number of freely circulating microbubbles per unit volume within the effective boundary layer near the bottom surface; d is the effective boundary layer thickness; N_{B} is the number of receptors (complementary to the ligands attached to microbubble shell) per unit area on the bottom surface of the vessel; k_{+} and k_{-} are reaction rate constants for association and disassociation process, respectively. Both reaction rate constants were expected to be functions of both ARF and flow shear force.

NIH-PA Author Manuscript

NIH-PA Author Manuscript

NIH-PA Author Manuscript

With application of constant ARF, freely circulating microbubble concentration within the effective boundary layer near the bottom surface increases. As a result, the concentration of adherent microbubbles increases. If surface concentration of receptors and flow velocity are constant, according to (2), N_{AMB} during application of ARF should be:

$$N_{\mathrm{AMB}}=\frac{k_{+}^{\mathrm{ON}}}{k_{-}^{\mathrm{ON}}}(N_{\mathrm{FMB}}^{\mathrm{ON}}d)N_{\mathrm{B}}-\left(\frac{k_{+}^{\mathrm{ON}}}{k_{-}^{\mathrm{ON}}}(N_{\mathrm{FMB}}^{\mathrm{ON}}d)N_{\mathrm{B}}-N_{\mathrm{AMB}}^{\mathrm{ON}}\right)\times e^{-\frac{t}{1/k_{-}^{\mathrm{ON}}}} \quad (3)$$

where $N_{\mathrm{FMB}}^{\mathrm{ON}}$ is the freely circulating microbubble concentration within the effective boundary layer near the bottom surface with application of ARF; $N_{\mathrm{AMB}}^{\mathrm{ON}}$ is the initial number of adherent microbubbles per unit area when ARF starts; k_{+}^{ON} and k_{-}^{ON} are reaction rate constants for association and disassociation process, respectively, with application of ARF. After cessation of ARF, concentration of freely circulating microbubbles within the effective boundary layer near the bottom surface decreases, resulting in a decaying signal magnitude. Assuming the acoustic pressure of imaging pulses is negligible, according to (2), N_{AMB} after cessation of ARF should be:

$$N_{\mathrm{AMB}}=\frac{k_{+}^{\mathrm{OFF}}}{k_{-}^{\mathrm{OFF}}}(N_{\mathrm{FMB}}^{\mathrm{OFF}}d)N_{\mathrm{B}}-\left(\frac{k_{+}^{\mathrm{OFF}}}{k_{-}^{\mathrm{OFF}}}(N_{\mathrm{FMB}}^{\mathrm{OFF}}d)N_{\mathrm{B}}-N_{\mathrm{AMB}}^{\mathrm{OFF}}\right)\times e^{-\frac{t}{1/k_{-}^{\mathrm{OFF}}}} \quad (4)$$

where $N_{\mathrm{FMB}}^{\mathrm{OFF}}$ is the freely circulating microbubble concentration within the effective boundary layer near the bottom surface after cessation of ARF; $N_{\mathrm{AMB}}^{\mathrm{OFF}}$ is the initial number of adherent microbubbles per unit area when ARF stops. k_{+}^{OFF} and k_{-}^{OFF} are reaction rate constants for association and disassociation process, respectively, after cessation of ARF.

In this study, the ultrasound signal magnitude, $M(t)$, is used as a quantity that is assumed to be directly proportional to adherent microbubble concentration. This assumption has been shown to be valid at low microbubble concentration and mechanical index (Dayton *et al* 2004, Caskey *et al* 2011, Deshpande *et al* 2010). According to (3), the signal magnitude dynamic response, $M_{\mathrm{rise}}(t)$, during application of ARF (figure 1) can be described as:

$$M_{\mathrm{rise}}(t)=M_{\mathrm{satu}}-(M_{\mathrm{satu}}-M_{\mathrm{init}})\times e^{-\frac{t}{\tau_{\mathrm{rise}}}} \quad (5)$$

where M_{init} is the initial signal magnitude before the application of ARF pulses; M_{satu} is the saturated signal magnitude after applying ARF for a sufficiently long time (*i.e.* after reaching steady-state); and τ_{rise} is the time constant. M_{init} and M_{satu} are proportional to $N_{\mathrm{AMB}}^{\mathrm{ON}}$ and $\frac{k_{+}^{\mathrm{ON}}}{k_{-}^{\mathrm{ON}}}(N_{\mathrm{FMB}}^{\mathrm{ON}}d)N_{\mathrm{B}}$, respectively. τ_{rise} equals to $1/k_{-}^{\mathrm{ON}}$. After cessation of ARF, according to (4), the decay section of signal magnitude curve, $M_{\mathrm{decay}}(t)$, can be described as:

$$M_{\mathrm{decay}}(t)=M_{\mathrm{resid}}-(M_{\mathrm{resid}}-M_{\mathrm{max}})\times e^{-\frac{t}{\tau_{\mathrm{decay}}}} \quad (6)$$

NIH-PA Author Manuscript

NIH-PA Author Manuscript

NIH-PA Author Manuscript

where M_{max} is the signal magnitude immediately after cessation of ARF; M_{resid} is the residual signal magnitude after reaching steady-state; and τ_{decay} is the time constant. M_{max} approaches M_{satu} as the time of ARF application goes to infinity. M_{max} and M_{resid} are proportional to $\frac{k_{+}^{\mathrm{OFF}}}{k_{-}^{\mathrm{OFF}}}(N_{\mathrm{FMB}}^{\mathrm{OFF}}d)N_{\mathrm{B}}$, respectively. τ_{rise} equals to $1/k_{-}^{\mathrm{OFF}}$.

2. Materials and Methods

2.1. In vitro experiment setup

Flow phantoms with liquid channels were used to mimic the elastic and acoustic properties of tissue (Hall *et al* 1997). 6.1 % (w/w) gelatin (Type B, Fisher Scientific, Pittsburgh, PA), 2.2 % (w/w) agar (Acros Organics, Geel, Belgium) and 1.8 % (w/w) graphite (< 20 μm, Sigma-Aldrich, St. Louis, MO) were dissolved in boiling water and then poured into a custom designed phantom holder (Applied Rapid Technologies, Fredericksburg, VA) at a temperature of 75 °C (figure 2). Borosilicate glass rods (McMaster-Carr, Robbinsville, NJ) with diameter of 4 mm were placed horizontally inside the phantom holder to mold liquid channels. The bottom of the embedded fluid channel was approximately 8 mm from the imaging surface of the flow phantom. To minimize the effects of inner liquid channel surface roughness on microbubble binding, all inner surfaces were examined optically and then observed under ultrasound to verify the presence of a smooth, specular reflecting, phantom wall. Targeted fluid channels were created using an incubation with 50 μg mL^{-1} streptavidin (AnaSpec, Fremont, CA) solution for 12 h followed by another incubation with 5 % (w/w) bovine serum albumin (BSA, Sigma-Aldrich, St. Louis, MO) for 1 h (Mauldin *et al* 2012). Control fluid channels were incubated with 5 % (w/w) BSA alone for 12 h. In this study, each fluid channel was used for one trial only (3 min of flowing microbubble solution).

Biotinylated lipid shelled microbubbles (mean diameter approximate 2.2 μm), synthesized in-house using existing methods (Klibanov *et al* 2006), were diluted in 0.9 % Sodium Chloride Irrigation, USP (Baxter Healthcare Corporation, Deerfield, IL) at concentrations of 0.1, 0.5, and 2.0 (10^6 mL^{-1}). Empirically, it has been shown that it is preferable to use acoustic radiation force for pushing those microbubbles at a transmit frequency of approximate 4 MHz (Patil *et al* 2011). BSA at 0.5 % (w/w) was added to the microbubble solution to further prevent non-specific adhesion (Hernot *et al* 2012). To maintain consistent microbubble concentration, a Coulter counter (Coulter Multisizer 3, Beckman Coulter Inc., Brea, CA) was used to determine the microbubble concentration immediately before experiments; and fresh microbubble solution was prepared every 10 min during experiments.

The ultrasound transducer (described below) used in these experiments was placed perpendicular to the bottom channel wall, which was located at a depth of 14 mm (figure 2). Experiments were performed by injecting microbubble solution through the fluid channels at flow velocities of 2, 6, and 10 cm s^{-1} (*i.e.* flow rates of 15.1, 45.2, and 75.4 mL min^{-1}, respectively) using a syringe pump (PHD 2000, Harvard Apparatus, Holliston, MA). The proposed flow velocities (2 – 10 cm s^{-1}) and vessel diameter (4 mm) in this study represented typical averaged flow velocities and vessel diameters of large human blood

NIH-PA Author Manuscript

NIH-PA Author Manuscript

NIH-PA Author Manuscript

vessels (*e.g.* brachial artery, averaged flow velocity ≈ 9 cm s^{-1}, averaged arterial diameter ≈ 4 mm) (Ku 1997, Safar *et al* 1981, Levenson *et al* 2000). Constant flow velocities and microbubble concentrations were maintained for 3 min while custom designed beam sequences (described below) were performed. Raw radiofrequency (RF) echo data was obtained for analysis of the adherent microbubble signal magnitude.

2.2. Custom designed beam sequence

Custom beam sequences were programmed on a Verasonics ultrasound scanner (Verasonics, Inc., Redmond, WA) equipped with an ATL L12-5 38 mm linear array transducer (Philips Healthcare, Andover, MA). For each trial, the sequence collected acoustic echo data continuously for 180 s at a frame rate of 4 Hz (figure 3). For each frame period (250 ms), three plane wave imaging pulses with a spacing of 200 μs were fired consecutively to obtain the acoustic echo data required to form one image frame. These three consecutive imaging pulses were identical. There was no amplitude or phase modulation performed. Focused A-lines were constructed by standard plane wave dynamic receive focusing methods (Foster *et al* 1989). From t = 10 s to 80 s, additional ARF pulses were inserted in each frame following the image pulses to increase microbubble binding efficiency along the bottom channel wall (Dayton *et al* 1999, 2002, Zhao *et al* 2004, Rychak *et al* 2005, 2007). The time interval between the ARF pulses and the following imaging pulses from the next frame was 175 ms – a sufficiently long time period for the system power supply to transition from a high voltage profile (5 V, ARF pulses) to a low voltage profile (1.6 V, imaging pulses). It was known *a priori* that adherent microbubbles would accumulate along the bottom channel wall under the ARF pulses as has been confirmed by fluorescent microscopy in previous studies (Patil *et al* 2011, Mauldin *et al* 2012). Average *PRF* of ARF pulses were chosen at 0.5, 2.5, and 5 kHz. A detailed list of parameters used for imaging and ARF pulses are provided in table 1. In order to minimize possible effects of imaging pulses on microbubble binding, the voltage applied to the transducer during imaging was maintained at the lowest programmable limit of the scanner, which gave a low mechanical index (MI) of 0.006 as confirmed with hydrophone measurements. In addition, the intensity of ARF pulses was optimized to provide sufficient pushing pressure (110.3 kPa) while maintaining a low MI of 0.05, which are below the published limits at which bursting occurs (Bouakaz *et al* 2005).

Consequently, the beam sequence was divided into three sections – 10 s of imaging (0 s ≤ t < 10 s), 70 s of imaging plus ARF applied (10 s ≤ t < 80 s), and 100 s of imaging (80 s ≤ t ≤ 180 s) – showing the baseline, rise, and decay of adherent microbubble concentration along the bottom channel wall.

2.3. In vitro experimental design framework

Experiments were designed to test the effects of flow velocity, microbubble concentration, and ARF on adherent microbubble signal magnitude curves. Flow and acoustic parameters of different groups are listed in table 2. The G_{Ref} label used throughout this paper represents the reference group, while G_{v1} and G_{v2} represent groups with a lower and a higher flow velocity compared to the G_{Ref} group, respectively. G_{C1} and G_{C2} represent groups with a lower and a higher microbubble concentration relative to the G_{Ref} group. G_{PRF1} and G_{PRF2} were two groups with lower *PRF* of ARF pulses compared to the G_{Ref} group, and therefore

NIH-PA Author Manuscript

NIH-PA Author Manuscript

NIH-PA Author Manuscript

a lower time averaged ARF intensity. For each group, experiments from 10 targeted and 10 control channels were performed. Each experiment was performed in a unique phantom channel in order to eliminate measurement bias that could result from phantom-to-phantom or batch-to-batch microbubble variations.

2.4. Quantitative analysis

Quantitative analysis was performed on focused acoustic echo data from 720 consecutive image frames. All analysis was performed in MATLAB (Mathworks, Natick, MA). For each trial, signal magnitude curves ($M(t)$, 0 s ≤ t ≤ 180 s) were obtained by calculating the average signal magnitude (after envelope detection of focused echo data) from regions of adherent microbubbles over time within the region of interest (ROI). The ROI was located at the center of the bottom channel wall and possessed a depth span of 0.2 mm and a lateral width of 2 mm. The following calculation was used to compute the averaged signal magnitude over the ROI:

$$M=\frac{1}{N_1 \times N_2}\left(\sum_{j=1}^{N_2}\sum_{i=1}^{N_1}\sqrt{I(i,j)^2+Q(i,j)^2}\right) \quad (7)$$

where $I(i, j)$ and $Q(i, j)$ are the real (in-phase) and imaginary (quadrature) components of the focused echo data within the ROI (dimension: $N_1 \times N_2$), respectively.

The depth of the ROI along the bottom channel wall was determined with an automated program that detected the location of maximum average signal magnitude over all image frames. The ROI spanned 10 consecutive laterally adjacent A-lines to increase measurement signal-to-noise. For each set of flow and acoustic conditions, 10 signal magnitude curves were calculated from 10 trials.

As described above, the initial signal magnitude (M_{init}), saturated signal magnitude (M_{satu}), maximum signal magnitude (M_{max}), residual signal magnitude (M_{resid}), time constant of rise (τ_{rise}) and decay (τ_{decay}) were the parameters used to characterize the signal magnitude curves of adherent microbubbles under the custom designed pulse sequences.

For signal magnitude curves (both from averaged and single trial), the second section ($M(t)$, 10 s ≤ t < 80 s) and the third section ($M(t)$, 80 s ≤ t ≤ 180 s) were used to fit (5) and (6), respectively, using the Curve Fitting Toolbox in MATLAB. Adjusted-R^2 values were used to evaluate the fitting performance. Parameters of M_{satu}, τ_{rise}, M_{resid} and τ_{decay} were obtained from curve fitting. The M_{init} parameter was obtained from the signal magnitude curve at t = 5 s. The M_{max} parameter was the maximum signal magnitude value during the entire 180 s period. For each set of flow and acoustic conditions, the fitting process was repeated over 10 trials. Thereafter, Student's t-tests were performed on those parameters among different sets of flow and acoustic conditions. Differences were considered statistical significant only if the calculated p-value was less than 0.05.

An additional signal magnitude curve parameter, ratio of residual to saturation signals (R_{resid}), was studied to assess its ability to detect targeted adhesion. The parameter is defined as:

NIH-PA Author Manuscript

NIH-PA Author Manuscript

NIH-PA Author Manuscript

$$R_{\text{resid}} = \left(\frac{M_{\text{resid}} - M_{\text{init}}}{M_{\text{satu}} - M_{\text{init}}}\right) \times 100\% \quad (8)$$

where M_{init} and M_{resid} are measured directly from the signal magnitude curve, $M(t)$, at $t = 5$ s and $t = 180$s, respectively; M_{satu} is the saturated signal magnitude after reaching steady-state. According to the model in (5), the M_{satu} parameter corresponds to full saturation of adherent microbubbles (both specific and non-specific binding) and the M_{init} parameter corresponds to background signal in absence of adherent microbubbles. According to the model in (6), only targeted ligand-receptor bound microbubbles remain after cessation of ARF. The concentration of remaining microbubbles are quantified by the M_{resid} parameter, which is bounded by M_{init} (lower bound) and M_{satu} (upper bound). Therefore, the R_{resid} value represents the percentage of these bounds that is spanned by the M_{resid} quantity. Because R_{resid} is not dependent on absolute signal magnitude levels, it is hypothesized in this study that it can provide more reliable detection of targeted adhesion independent of control measurements.

3. Results

3.1. Effects of control and targeted channels on signal magnitude curves

Representative signal magnitude curves observed during the modulated ARF pulse sequence are illustrated in figure 4(a) (default imaging conditions listed as the G_{Ref} group in table 2). The curves represent the average over 10 trials for both control and targeted experiments. In both curves, during the first 10 s period with no application of ARF, there was no significant change of signal magnitude ($p > 0.2$, n = 10). During the next 70 s period, with application of ARF, the signal magnitude for both control and targeted channels exponentially approached a steady-state magnitude in excellent agreement with the proposed model (adjusted-R^2 value of 0.99 to fit (5)). During the last 100 s period after cessation of ARF, the signal magnitude of targeted channels exhibited an exponential decay to a residual level, again in excellent agreement with the proposed model (adjusted-R^2 value of 0.97 to fit (6)). However, in the control channels, an immediate increase in signal magnitude ("control peak") was observed after cessation of ARF. As will be further illustrated below, the control peak observation was consistent across a wide of range of flow rates, microbubble concentrations, and ARF investigated in this study. After reaching the control peak (t = 84.50 s), the control curve demonstrated the same exponential decay to a residual level as observed in the targeted example (adjusted-R^2 value of 0.96 to fit (6)). For illustration of these trends, corresponding B-mode images (one trial) from both control and targeted channels are provided. Images show the ROI (yellow boxes) at different time points in figure 4: (b) control, t = 5.00 s; (c) targeted, t = 5.00 s; (d) control, t = 80.00 s; (e) targeted, t = 80.00 s; (f) control, t = 84.50 s; (g) targeted, t = 84.50 s; (h) control, t = 180.00 s; and (i) targeted, t = 180.00 s.

For flow and acoustic conditions of other groups in table 2, the averaged signal magnitude curves for control and targeted channels are illustrated in figure 5. For the six different groups (G_{v1}, G_{v2}, G_{C1}, G_{C2}, G_{PRF1}, G_{PRF2}), the region of the signal magnitude curve (both control and targeted) with application of ARF (10 s ≤ t < 80 s) fit (5) with a minimum

NIH-PA Author Manuscript

NIH-PA Author Manuscript

NIH-PA Author Manuscript

adjusted-R^2 value of 0.95. The "control peak" of signal magnitude curves for control channels was observed in all six groups at different times (G_{v1}, t = 90.75 s; G_{v2}, t = 82.50 s; G_{C1}, t = 83.00 s; G_{C2}, t = 85.50 s; G_{PRF1}, t = 85.00 s; G_{PRF2}, t = 84.50 s). Hence, for control channels, the curve fit following application of ARF to (6) started from the time of the "control peak" to the end of the signal magnitude curve (t = 180 s); for targeted channels, the range was from 80 s to 180 s. The minimum adjusted-R^2 value from these experiments was 0.92 except for the G_{C2} group (adjusted-R^2 = 0.89 for control and 0.71 for targeted channels).

3.2. Effects of flow velocities on signal magnitude curves

The effects of flow velocities on parameters (M_{init}, M_{satu}, M_{resid}, τ_{rise}, τ_{decay}) of signal magnitude curves for groups of G_{v1}, G_{Ref}, and G_{v2} are presented in figure 6. According to table 2, flow velocity was the only parameter varied among these three groups. The M_{init} parameter increased monotonically with flow velocity, with a significant difference between the minimum and maximum M_{init} ($p < 0.001$, n = 10) (figure 6(a)). In the G_{v2} group, the M_{satu} parameter for control channel was significantly higher than that of targeted ($p < 0.01$, n = 10) (figure 6(b)). The M_{resid} parameter of targeted channel was significantly higher than that of control for all three groups of G_{v1}, G_{Ref}, and G_{v2} ($p < 0.01$, $p < 0.001$, and $p < 0.001$, correspondingly; n = 10) (figure 6(c)). There was no significant difference of the τ_{rise} parameter between control and targeted channels for all three groups (figure 6(d)). The τ_{decay} parameter of targeted channel was significantly higher than that of control channels in groups G_{v1} and G_{v2} ($p < 0.001$, and $p < 0.01$, correspondingly; n = 10) (figure 6(e)). In addition, the τ_{decay} parameter of targeted channels decreased monotonically with flow velocity, with a significant difference observed between the minimum and maximum τ_{decay} ($p < 0.001$, n = 10).

3.3. Effects of microbubble concentrations on signal magnitude curves

The effects of microbubble concentration on parameters (M_{init}, M_{satu}, M_{resid}, τ_{rise}, τ_{decay}) for groups G_{C1}, G_{Ref}, and G_{C2} are presented in figure 7. Microbubble concentration was the only parameter varied among these three groups (table 2). The M_{init} parameter of both control and targeted channels monotonically decreased with microbubble concentration, with a significant difference observed between the minimum and maximum M_{init} ($p < 0.001$, n = 10) (figure 7(a)). The M_{satu} parameter in the G_{C2} group was significantly lower than the other two groups ($p < 0.001$, n = 10) (figure 7(b)). The M_{resid} parameter of targeted channels were significantly higher than that of control channels for all three groups G_{C1}, G_{Ref}, and G_{C2} ($p < 0.01$, $p < 0.001$, and $p < 0.001$, correspondingly; n = 10) (figure 7(c)). In addition, the M_{resid} parameter of control channels monotonically decreased with microbubble concentration, with a significant difference observed between the minimum and maximum M_{resid} ($p < 0.001$, n = 10). There was no significant difference for the τ_{rise} parameter between control and targeted channels in groups G_{C1} and G_{Ref} (figure 7(d)). No significant difference of the τ_{decay} parameter was found between control and targeted channels for all three groups. However, the τ_{decay} parameter of both control and targeted channels monotonically decreased with microbubble concentration.

NIH-PA Author Manuscript

NIH-PA Author Manuscript

NIH-PA Author Manuscript

3.4. Effects of time-averaged ARF on signal magnitude curves

The effects of ARF on parameters (M_{init}, M_{satu}, M_{resid}, τ_{rise}, τ_{decay}) for groups G_{PRF1}, G_{PRF2} and G_{Ref} are presented in figure 8. *PRF* was the only parameter varied among these three groups (table 2). No significant difference for the M_{init} parameter was found between control and targeted channels among different groups (figure 8(a)). There was no significant difference for the M_{satu} parameter between control and targeted channels (figure 8(b)). The difference between minimum and maximum M_{satu} was significant ($p < 0.01$ for control, $p < 0.05$ for targeted, $n = 10$). The M_{resid} parameter from targeted channel experiments was significantly higher than for all three groups G_{PRF1}, G_{PRF2} and G_{Ref} ($p < 0.05$, $p < 0.001$, and $p < 0.001$, correspondingly; n = 10) (figure 8(c)). In addition, the M_{resid} parameter of targeted channel experiments increased monotonically with *PRF*, with significant difference between the minimum and maximum M_{resid} ($p < 0.001$, n = 10). The τ_{rise} parameter for both control and targeted channels decreased monotonically with *PRF*, with significant difference between the minimum and maximum τ_{rise} ($p < 0.001$, n = 10) (figure 8(d)). The τ_{decay} parameter of targeted channel was significantly higher than that for groups of G_{PRF1} and G_{PRF2} ($p < 0.05$, n = 10) (figure 8 (e)). In addition, the τ_{decay} parameter from control channel experiments increased monotonically with *PRF*, with significant difference between the minimum and maximum τ_{decay} ($p < 0.05$, n = 10).

3.5. R_{resid} under different experimental conditions

The R_{resid} parameter observed for control and targeted channels across the various experimental conditions are presented in figure 9. For control channels at different groups, the R_{resid} parameter was not significantly higher than zero ($p > 0.2$) or significantly lower than zero ($p < 0.05$) except for groups of G_{v1} and G_{C1} ($p < 0.05$; R_{resid} = 2.3 % and 7.6 %, respectively). For targeted channels, the R_{resid} parameter was significantly higher than zero and remained above 10 % except for the G_{PRF1} group ($p = 0.057$, R_{resid} = 5.9 %). The maximum R_{resid} of targeted channel (41.8 %) occurred in the G_{C2} group. For every experimental condition tested in this study, the difference between R_{resid} values of the control and targeted channels were statistically significant ($p < 0.01$ for G_{PRF1}, $p < 0.001$ for all other groups, n = 10).

4. Discussion

In this paper, an empirical model for binding dynamics of targeted microbubbles in response to a custom-designed modulated ARF pulse sequence was presented. Experiments were designed and executed systematically to examine the model and study the effects of flow velocity, microbubble concentration, and time-averaged ARF on binding dynamics. Different parameters extracted from the signal magnitude curves of adherent microbubbles were assessed for their ability to differentiate specific from non-specific binding. The ratio of residual to saturation signal (R_{resid}), which was only quantifiable using a modulated ARF sequence, was found to best detect targeted adhesion, especially compared with observing the signal magnitude alone in absence of modulated ARF. The primary focus of the modulated acoustic radiation force method proposed in this study is for targeted molecular imaging in large blood vessel environments, such as in the carotid or abdominal aorta.

NIH-PA Author Manuscript

NIH-PA Author Manuscript

NIH-PA Author Manuscript

Generally, the shape of magnitude curve of targeted channels exhibited a good fit to the model as illustrated in figure 1. In control experiments, the "control peak" observed experimentally after cessation of ARF was not predicted by the model. One possible explanation for the "control peak" is related to the effects of aggregating non-specifically bound adherent microbubbles. After cessation of ARF, most adherent microbubbles in targeted channels remained attached at the bottom channel wall due to molecular binding and flow shear forces gradually removed a small portion of targeted adherent microbubbles. However, for control channels, the majority of microbubbles detached from the bottom wall and moved upward due to buoyancy forces immediately after the cessation of ARF. Simultaneously, this layer of microbubbles were washed away and aggregated due to flow shear forces. Consequently, this sudden aggregation of microbubbles along vessel wall resulted in signal magnitude increase – "control peak". Additional experiments using optical observation are needed to verify the cause of the "control peak". This "control peak" could potentially be used to separate non-specific and specific binding of adherent microbubbles.

4.1. Effects of flow and acoustic conditions on signal magnitude curves

The effects of flow velocity, microbubble concentration, and ARF on signal magnitude curves are summarized in table 3. In flow velocity experiments (figure 6), the τ_{decay} parameter in targeted channels decreased with flow velocity, indicating that molecularly bound adherent microbubbles were washed away more quickly with higher flow shear forces. The M_{init} parameter decreased with microbubble concentration (figure 7) due to a strong shadowing effect that was easily observed in the resulting images. The shadowing is derived from attenuation produced by microbubbles in the channel, which dampens the overall signal magnitude along the bottom channel wall (Klibanov 1999). There was an observed threshold of microbubble concentration between 0.5 and 2.0×10^6 mL^{-1}, above which the M_{satu} and M_{resid} parameters (targeted) decreased because of excessive shadowing effects from high concentrations of microbubbles. In addition, the τ_{decay} parameter decreased with microbubble concentration for both targeted and control, suggesting that high microbubble concentration led to a higher reaction rate of the detaching process. The M_{satu} and M_{resid} parameters (targeted) increased with *PRF* (figure 8) due to increased quantity of microbubbles being pushed to lower channel wall and because the steady-state assumption was better satisfied. The τ_{rise} parameter decreased with *PRF*, suggesting that higher intensity of ARF would increase the reaction rate of microbubble attaching process.

4.2. On the potential of R_{resid} as an ideal parameter for quantitative detection targeted adhesion independent of control measurement

Results illustrated that M_{resid} is the best parameter among the three parameters (M_{satu}, τ_{decay}, and M_{resid}) that were considered for detecting specific versus non-specific binding of adherent microbubbles (see Appendix). In addition, results demonstrated the R_{resid} parameter as a potentially more quantitative parameter that would be independent of absolute signal magnitude and thereby more immune to variabilities in tissue attenuation (figure 9). The R_{resid} parameter quantity typically ranges between 0 % and 100 % and represents a percentage of the total wall surface that retains molecularly targeted microbubbles. This interpretation assumes the following assumptions. First, signal magnitude is proportional to microbubble concentration. Second, the M_{init} parameter is the

NIH-PA Author Manuscript

NIH-PA Author Manuscript

NIH-PA Author Manuscript

reflection magnitude of the vessel wall without adherent microbubble signal. Third, the M_{satu} parameter is the reflection magnitude when the vessel wall area is completely saturated with adherent microbubbles (including both non-specifically and specifically bound microbubbles). Fourth, most non-specifically bound adherent microbubbles leave the vessel wall with cessation of radiation force while most specifically bound adherent microbubbles remain. Results in this study demonstrated that R_{resid} of targeted experiments were significantly higher than zero and remained above 10 % for all groups except in the G_{PRF1} group. This exception was due to an overall lower concentration of microbubbles attached on the wall caused by insufficient ARF (*i.e.* the third assumption listed above was not valid because steady-state was not reached). In control experiments, the R_{resid} parameter remained below 10 % for all groups. Even though the above four assumptions were not directly verified in this study, it was determined that R_{resid} was the best parameter for detecting specific versus non-specific binding and R_{resid}, by definition, is independent of absolute signal magnitude. The results also suggest that the value of R_{resid} was an excellent predictor of targeted adhesion without the requirement for a control measurement. This finding was especially true if sufficiently high microbubble concentration and *PRF* were used. In these instances, any R_{resid} above 10% was representative of targeted adhesion.

The results in figure 9 also show that flow shear forces, microbubble concentration and ARF played a big role in R_{resid} values of targeted channels. Even with the same ligand concentration on the vessel wall (controlled in the experimental setup), the R_{resid} parameter in the G_{v2} group was lower than that in the G_{Ref} group due to high flow shear forces, which led to higher detachment of specifically bound microbubbles. Therefore, the R_{resid} parameter is generally an underestimation of the percentage of wall covered by targeted ligands. Because the R_{resid} parameter is independent of absolute signal magnitude and related to the concentration of ligand coverage along the vessel wall, it can potentially be used for quantitative targeted molecular imaging with the need for control experiments. In future work, we will focus on validating the R_{resid} parameter with the goal of achieving fast, quantitative measurements related to ligand concentration without the need for multiple microbubble populations.

5. Conclusions

In summary, the empirical model provided for binding dynamics of targeted microbubbles in response to modulated ARF pulse sequences was demonstrated to be consistent with experimental results. Higher flow velocity and microbubble concentration led to faster detaching rates of specifically bound adherent microbubbles after cessation of ARF. Higher time-average ARF led to faster attaching rate and higher saturation magnitudes during the application of ARF. The residual microbubble magnitude (M_{resid}) of targeted channels was significantly higher than that of control channels at all flow and acoustic conditions in this study. The ratio of residual to saturation signal (R_{resid}) was observed to be an excellent parameter for detection of targeted adhesion without the need for separate control measurements. If certain assumptions are met, then R_{resid} provides a quantity related to the percentage of remaining specifically bound adherent microbubbles along the vessel wall. Therefore, these results suggest that modulated ARF sequences and extraction of the R_{resid} parameter has potential for use in targeted molecular imaging and as a means to achieve

NIH-PA Author Manuscript

NIH-PA Author Manuscript

NIH-PA Author Manuscript

quantitative measures of ligand concentration in real-time, using relatively short imaging protocols (approximately 3 min) that do not require separate control populations or waiting periods.

Acknowledgments

This work was supported by NIH R01 EB001826 and R01 HL111077. The content is solely the responsibility of the authors and does not necessarily represent the official views of the NIH. The authors would like to thank Claudia Y. Wang for her help with the experiments; Sunil Unnikrishnan for his advice related to microbubbles and flow phantom experiments; and Verasonics, Inc. for their technical support.

Appendix

Specificity of magnitude curve parameters for detection of targeted versus control

Three parameters extracted directly from the single magnitude curves (M_{satu}, τ_{decay}, and M_{resid}) could potentially be used to differentiate specific from non-specific binding of adherent microbubbles. Typical approaches to real-time targeted molecular imaging seek to quantify the presence of specifically bound adherent microbubbles without modulating ARF. In these approaches, the image intensity of targeted microbubbles at a given time is measured and compared against control. The M_{satu} parameter is an example of a parameter used in standard approaches. In contrast, the dynamic response of adherent microbubbles under modulated ARF is closely related to the binding strength of ligand-receptor pairs. Specifically bound adherent microbubbles have much higher binding strength than non-specifically bound ones, and therefore require higher external forces (buoyancy force, flow shear force, *etc.*) to detach. As a result, after the cessation of ARF, the remaining number of specifically bound microbubbles (proportional to M_{resid}) was hypothesized to be higher than that of non-specifically bound microbubbles.

Table A1

Parameter ability to differentiate targeted from control

Parameter	Group		
	G_{v1}, G_{Ref}, G_{v2} (figure 6)	G_{C1}, G_{Ref}, G_{C2} (figure 7)	G_{PRF1}, G_{PRF2}, G_{Ref} (figure 8)
M_{satu}	–[a]	–	–
τ_{decay}	–	–	–
M_{resid}	+[b]	+	+

[a] No significant difference between targeted and control among all three corresponding groups

[b] Significant difference between targeted and control among all three corresponding groups

The results of the three parameters (M_{satu}, τ_{decay}, and M_{resid}) for both targeted and control are summarized in table A1. Among the three parameters, only the M_{resid} parameter exhibited consistent significant differences between targeted and control under all flow and acoustic conditions listed in table 2. It was therefore the best parameter for detecting specific versus non-specific binding of adherent microbubbles. Note that in other proposed real-time

NIH-PA Author Manuscript

NIH-PA Author Manuscript

NIH-PA Author Manuscript

approaches, a parameter related to M_{satu} is typically used as a measure of molecular marker presence (Nitta-Seko *et al* 2010, Masseau *et al* 2012, Patil *et al* 2009, Mauldin *et al* 2012). In these experiments, we observed that the M_{satu} parameter was not a reliable indicator of targeted binding. Instead, modulation of ARF with measures of M_{resid} was required to distinguish targeted versus control.

References

Bell G. Models for the specific adhesion of cells to cells. Science. 1978; 200:618–627. [PubMed: 347575]

Bhatia SK, King MR, Hammer DA. The State Diagram for Cell Adhesion Mediated by Two Receptors. Biophys J. 2003; 84:2671–2690. [PubMed: 12668476]

Bouakaz A, Versluis M, de Jong N. High-speed optical observations of contrast agent destruction. Ultrasound Med Biol. 2005; 31:391–399. [PubMed: 15749563]

Caskey CF, Hu X, Ferrara KW. Leveraging the power of ultrasound for therapeutic design and optimization. J Control Release. 2011; 156:297–306. [PubMed: 21835212]

Chang KC, Hammer DA. Adhesive dynamics simulations of sialyl-Lewis(x)/E-selectin-mediated rolling in a cell-free system. Biophys J. 2000; 79:1891–1902. [PubMed: 11023895]

Dayton PA, Allen JS, Ferrara KW. The magnitude of radiation force on ultrasound contrast agents. J Acoust Soc Am. 2002; 112:2183–2192. [PubMed: 12430830]

Dayton PA, Ferrara KW. Targeted imaging using ultrasound. J Magn Reson Imaging. 2002; 16:362–377. [PubMed: 12353252]

Dayton PA, Pearson D, Clark J, Simon S, Schumann PA, Zutshi R, Matsunaga TO, Ferrara KW. Ultrasonic analysis of peptide- and antibody-targeted microbubble contrast agents for molecular imaging of alphavbeta3-expressing cells. Mol Imaging. 2004; 3:125–134. [PubMed: 15296677]

Dayton P, Klibanov A, Brandenburger G, Ferrara K. Acoustic radiation force in vivo: a mechanism to assist targeting of microbubbles. Ultrasound Med Biol. 1999; 25:1195–1201. [PubMed: 10576262]

Deshpande N, Needles A, Willmann JK. Molecular ultrasound imaging: current status and future directions. Clin Radiol. 2010; 65:567–581. [PubMed: 20541656]

Ferrante EA, Pickard JE, Rychak J, Klibanov A, Ley K. Dual targeting improves microbubble contrast agent adhesion to VCAM-1 and P-selectin under flow. J Control Release. 2009; 140:100–107. [PubMed: 19666063]

Ferrara K, Pollard R, Borden M. Ultrasound microbubble contrast agents: fundamentals and application to gene and drug delivery. Annu Rev Biomed Eng. 2007; 9:415–447. [PubMed: 17651012]

Foster FS, Larson JD, Mason MK, Shoup TS, Nelson G, Yoshida H. Development of a 12 element annular array transducer for realtime ultrasound imaging. Ultrasound Med Biol. 1989; 15:649–659. [PubMed: 2683291]

Gessner RC, Streeter JE, Kothadia R, Feingold S, Dayton Pa. An in vivo validation of the application of acoustic radiation force to enhance the diagnostic utility of molecular imaging using 3-d ultrasound. Ultrasound Med Biol. 2012; 38:651–660. [PubMed: 22341052]

Hall TJ, Bilgen M, Insana MF, Krouskop TA. Phantom materials for elastography. IEEE Trans. Ultrason. Ferroelectr. Freq. Control. 1997; 44:1355–1365.

Hammer DA, Lauffenburger DA. A dynamical model for receptor-mediated cell adhesion to surfaces in viscous shear flow. Cell Biophys. 1989; 14:139–173. [PubMed: 2472206]

Hernot S, Klibanov AL. Microbubbles in ultrasound-triggered drug and gene delivery. Adv Drug Deliv Rev. 2008; 60:1153–1166. [PubMed: 18486268]

Hernot S, Unnikrishnan S, Du Z, Shevchenko T, Cosyns B, Broisat A, Toczek J, Caveliers V, Muyldermans S, Lahoutte T, Klibanov AL, Devoogdt N. Nanobody-coupled microbubbles as novel molecular tracer. J Control Release. 2012; 158:346–353. [PubMed: 22197777]

NIH-PA Author Manuscript NIH-PA Author Manuscript NIH-PA Author Manuscript

Hu X, Caskey CF, Mahakian LM, Kruse DE, Beegle JR, Declèves A-E, Rychak JJ, Sutcliffe PL, Sharma K, Ferrara KW. In vivo validation and 3D visualization of broadband ultrasound molecular imaging. Am J Nucl Med Mol Imaging. 2013; 3:336–349. [PubMed: 23901359]

Hu X, Zheng H, Kruse DE, Sutcliffe P, Stephens DN, Ferrara KW. A sensitive TLRH targeted imaging technique for ultrasonic molecular imaging. IEEE Trans. Ultrason. Ferroelectr. Freq. Control. 2010; 57:305–316. [PubMed: 20178897]

De Jong N, Hoff L, Skotland T, Bom N. Absorption and scatter of encapsulated gas filled microspheres: theoretical considerations and some measurements. Ultrasonics. 1992; 30:95–103. [PubMed: 1557838]

Klibanov A. Targeted delivery of gas-filled microspheres, contrast agents for ultrasound imaging. Adv Drug Deliv Rev. 1999; 37:139–157. [PubMed: 10837732]

Klibanov A. Ultrasound contrast agents: development of the field and current status. Contrast Agents II. 2002; 222:73–106.

Klibanov AL. Ultrasound molecular imaging with targeted microbubble contrast agents. J Nucl Cardiol. 2007; 14:876–884. [PubMed: 18022115]

Klibanov AL, Hughes MS, Marsh JN, Hall CS, Miller JG, Wible JH, Brandenburger GH. Targeting of ultrasound contrast material. An in vitro feasibility study. Acta Radiol Suppl. 1997; 412:113–120. [PubMed: 9240089]

Klibanov AL, Muzykantov VR, Ivanov NN, Torchilin VP. Evaluation of quantitative parameters of the interaction of antibody-bearing liposomes with target antigens. Anal Biochem. 1985; 150:251–257. [PubMed: 4091252]

Klibanov AL, Rychak JJ, Yang WC, Alikhani S, Li B, Acton S, Lindner JR, Ley K, Kaul S. Targeted ultrasound contrast agent for molecular imaging of inflammation in high-shear flow. Contrast Media Mol Imaging. 2006; 1:259–266. [PubMed: 17191766]

Krasik EF, Yee KL, Hammer DA. Adhesive dynamics simulation of neutrophil arrest with deterministic activation. Biophys J. 2006; 91:1145–1155. [PubMed: 16731552]

Ku DN. Blood Flow in Arteries. Annu Rev Fluid Mech. 1997; 29:399–434.

Levenson JA, Peronneau PA, Simon A, Safar ME. Pulsed Doppler: determination of diameter, blood flow velocity, and volumic flow of brachial artery in man. Cardiovasc Res. 2000; 45:23–26. [PubMed: 10728308]

Lindner JR. Microbubbles in medical imaging: current applications and future directions. Nat Rev Drug Discov. 2004a; 3:527–532. [PubMed: 15173842]

Lindner JR. Molecular imaging with contrast ultrasound and targeted microbubbles. J Nucl Cardiol. 2004b; 11:215–221. [PubMed: 15052252]

Lindner JR, Song J, Christiansen J, Klibanov AL, Xu F, Ley K. Ultrasound assessment of inflammation and renal tissue injury with microbubbles targeted to P-selectin. Circulation. 2001; 104:2107–2112. [PubMed: 11673354]

Lindner JR, Song J, Xu F, Klibanov aL, Singbartl K, Ley K, Kaul S. Noninvasive Ultrasound Imaging of Inflammation Using Microbubbles Targeted to Activated Leukocytes. Circulation. 2000; 102:2745–2750. [PubMed: 11094042]

Masseau I, Davis MJ, Bowles DK. Carotid inflammation is unaltered by exercise in hypercholesterolemic Swine. Med Sci Sports Exerc. 2012; 44:2277–2289. [PubMed: 22776877]

Maul TM, Dudgeon DD, Beste MT, Hammer DA, Lazo JS, Villanueva FS, Wagner WR. Optimization of ultrasound contrast agents with computational models to improve selection of ligands and binding strength. Biotechnol Bioeng. 2010; 107:854–864. [PubMed: 20665479]

Mauldin FWJ, Dhanaliwala AH, Patil AV, Hossack JA. Real-time targeted molecular imaging using singular value spectra properties to isolate the adherent microbubble signal. Phys Med Biol. 2012; 57:5275–5293. [PubMed: 22853933]

Mayer CR, Bekeredjian R. Ultrasonic gene and drug delivery to the cardiovascular system. Adv Drug Deliv Rev. 2008; 60:1177–1192. [PubMed: 18474407]

Needles A, Couture O, Foster FS. A method for differentiating targeted microbubbles in real time using subharmonic micro-ultrasound and interframe filtering. Ultrasound Med Biol. 2009; 35:1564–1573. [PubMed: 19632763]

NIH-PA Author Manuscript

NIH-PA Author Manuscript

NIH-PA Author Manuscript

Nitta-Seko A, Nitta N, Shiomi M, Sonoda A, Ota S, Tsuchiya K, Takahashi M, Fujimiya M, Kiyoshi M. Utility of contrast-enhanced ultrasonography for qualitative imaging of atherosclerosis in Watanabe heritable hyperlipidemic rabbits: initial experimental study. Jpn J Radiol. 2010; 28:656–662. [PubMed: 21113749]

Patil AV, Rychak JJ, Allen JS, Klibanov AL, Hossack JA. Dual frequency method for simultaneous translation and real-time imaging of ultrasound contrast agents within large blood vessels. Ultrasound Med Biol. 2009; 35:2021–2030. [PubMed: 19828229]

Patil AV, Rychak JJ, Klibanov AL, Hossack JA. Real-time technique for improving molecular imaging and guiding drug delivery in large blood vessels: in vitro and ex vivo results. Mol Imaging. 2011; 10:238–247. [PubMed: 21521555]

Phillips P. Contrast pulse sequences (CPS): imaging nonlinear microbubbles. IEEE Ultrason. Symp. 2001:1739–1745.

Phillips P, Gardner E. Contrast-agent detection and quantification. Eur Radiol. 2004; 14(Suppl 8):P4–P10. [PubMed: 15700327]

Pochon S, Tardy I, Bussat P, Bettinger T, Brochot J, Von Wronski M, Passantino L, Schneider M. BR55: a lipopeptide-based VEGFR2-targeted ultrasound contrast agent for molecular imaging of angiogenesis. Invest Radiol. 2010; 45:89–95. [PubMed: 20027118]

Pysz, Ma; Guracar, I.; Foygel, K.; Tian, L.; Willmann, JK. Quantitative assessment of tumor angiogenesis using real-time motion-compensated contrast-enhanced ultrasound imaging. Angiogenesis. 2012a; 15:433–442. [PubMed: 22535383]

Pysz MA, Guracar I, Tian L, Willmann JK. Fast microbubble dwell-time based ultrasonic molecular imaging approach for quantification and monitoring of angiogenesis in cancer. Quant Imaging Med Surg. 2012b; 2:68–80. [PubMed: 22943043]

Rychak JJ, Klibanov AL, Hossack JA. Acoustic radiation force enhances targeted delivery of ultrasound contrast microbubbles: in vitro verification. IEEE Trans. Ultrason. Ferroelectr. Freq. Control. 2005; 52:421–433. [PubMed: 15857050]

Rychak JJ, Klibanov AL, Ley KF, Hossack JA. Enhanced targeting of ultrasound contrast agents using acoustic radiation force. Ultrasound Med Biol. 2007; 33:1132–1139. [PubMed: 17445966]

Safar ME, Peronneau PA, Levenson JA, Toto-Moukouo JA, Simon AC. Pulsed Doppler: diameter, blood flow velocity and volumic flow of the brachial artery in sustained essential hypertension. Circulation. 1981; 63:393–400. [PubMed: 7449061]

Stieger SM, Dayton PA, Borden MA, Caskey CF, Griffey SM, Wisner ER, Ferrara KW. Imaging of angiogenesis using Cadence contrast pulse sequencing and targeted contrast agents. Contrast Media Mol Imaging. 2008; 3:9–18. [PubMed: 18335479]

Takalkar AM, Klibanov AL, Rychak JJ, Lindner JR, Ley K. Binding and detachment dynamics of microbubbles targeted to P-selectin under controlled shear flow. J Control Release. 2004; 96:473–482. [PubMed: 15120903]

Unnikrishnan S, Klibanov AL. Microbubbles as ultrasound contrast agents for molecular imaging: preparation and application. AJR Am J Roentgenol. 2012; 199:292–299. [PubMed: 22826389]

Wang S, Mauldin FWJ, Klibanov AL, Hossack JA. Shear Forces from Flow are Responsible for a Distinct Statistical Signature of Adherent Microbubbles in Large Vessels. Mol Imaging. 2013; 12:396–408. [PubMed: 23981785]

Zhao S, Borden M, Bloch SH, Kruse D, Ferrara KW, Dayton PA. Radiation-force assisted targeting facilitates ultrasonic molecular imaging. Mol Imaging. 2004; 3:135–148. [PubMed: 15530249]

NIH-PA Author Manuscript

NIH-PA Author Manuscript

NIH-PA Author Manuscript

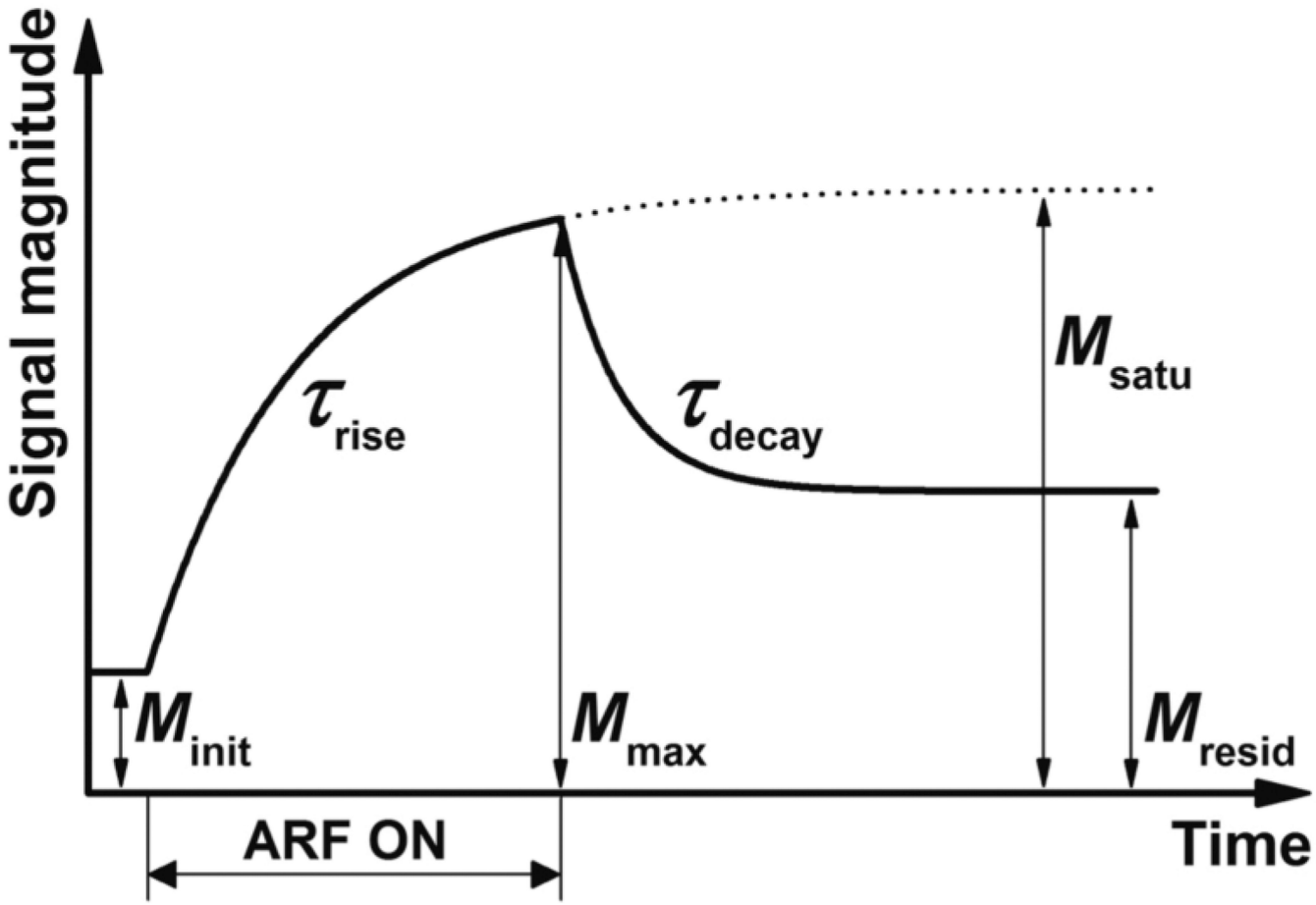

Figure 1.

A representative ultrasound signal magnitude curve determined by (5) and (6) in response to a modulated ARF input. Corresponding signal magnitude parameters of the response are labeled. The ultrasound signal magnitude was assumed to be directly proportional to microbubble concentration of adherent microbubbles along the bottom vessel wall.

NIH-PA Author Manuscript

NIH-PA Author Manuscript

NIH-PA Author Manuscript

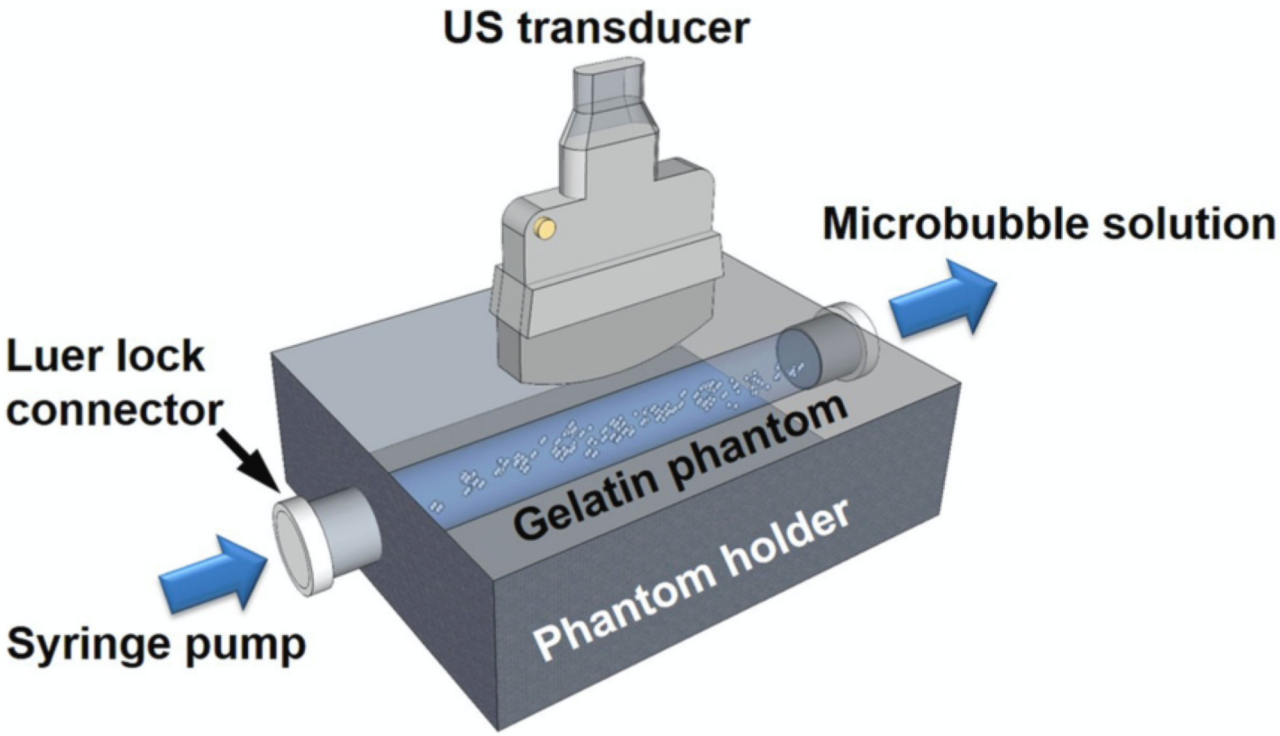

Figure 2.
The *in vitro* experimental setup.

NIH-PA Author Manuscript

NIH-PA Author Manuscript

NIH-PA Author Manuscript

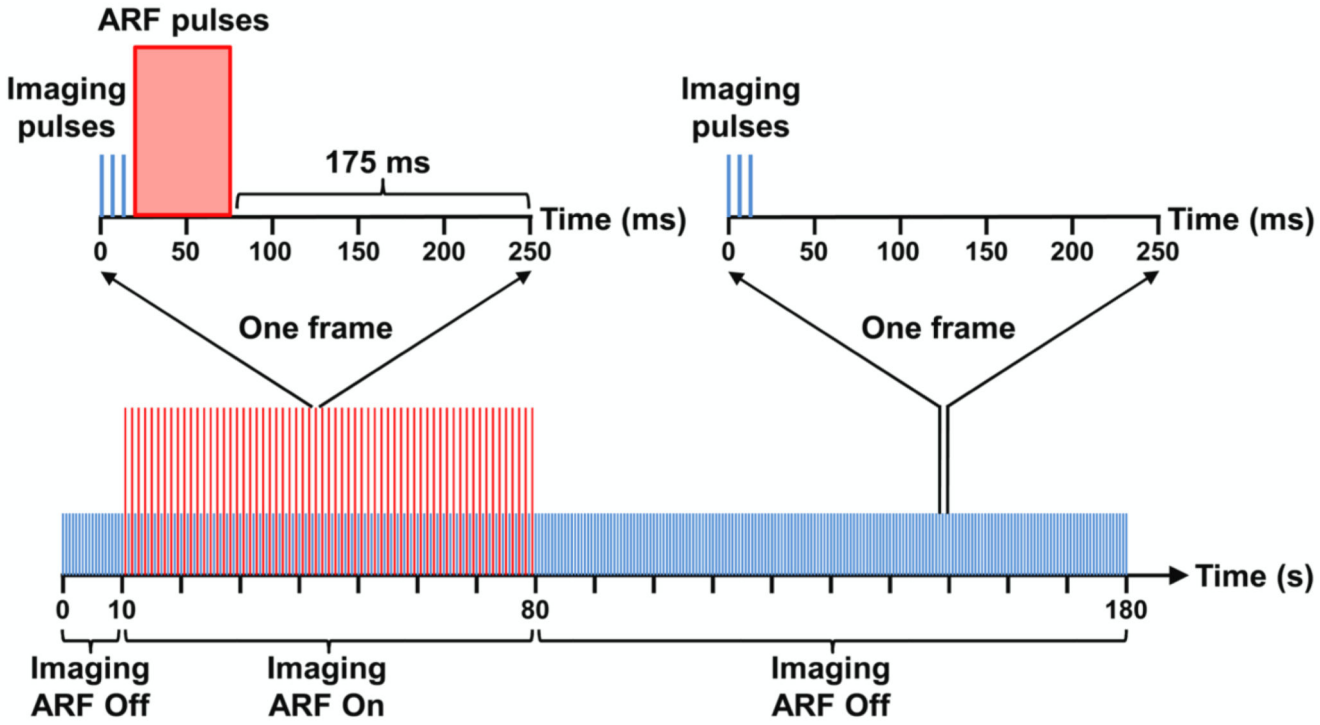

Figure 3.

Diagram of the custom designed beam sequence for modulated ARF. Imaging and ARF pulses are represented with blue and red colors, respectively. The amplitudes of imaging and ARF pulses are not to scale.

NIH-PA Author Manuscript

NIH-PA Author Manuscript

NIH-PA Author Manuscript

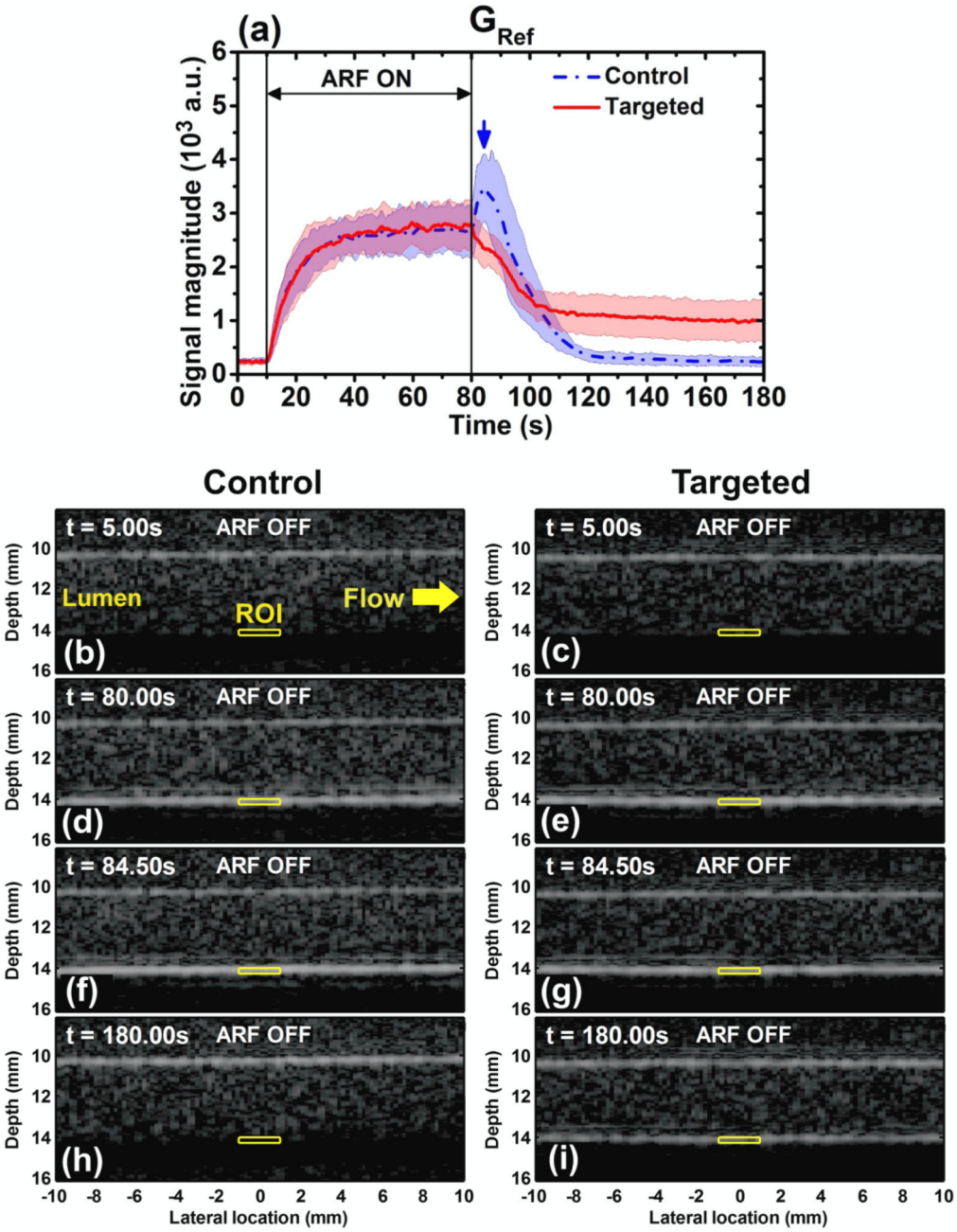

Figure 4.

(a) Averaged signal magnitude curves for control channel (blue) and targeted channel (red) at the acoustic and flow conditions of the reference group, G_{Ref} (table 2). Blue dash-dot and red solid lines indicate the mean values from 10 trials. Light color shadows indicate the corresponding error bars at the range of [mean ± standard deviation]. The blue arrow shows the peak of the signal magnitude curve in control channel at t = 84.50 s. B-mode images were displayed at 50 dB dynamic range show the channel lumen of control and targeted channel at different times: (b) control, t = 5.00 s; (c) targeted, t = 5.00 s; (d) control, t =

NIH-PA Author Manuscript

NIH-PA Author Manuscript

NIH-PA Author Manuscript

80.00 s; (e) targeted, t = 80.00 s; (f) control, t = 84.50 s (peak); (g) targeted, t = 84.50 s; (h) control, t = 180.00 s; (i) targeted, t = 180.00 s. Yellow windows indicate the region of interest (ROI) with dimensions of 2 mm × 0.2 mm. Microbubble solution flowed from left to right at a velocity of 6.0 cm s^{-1}.

NIH-PA Author Manuscript

NIH-PA Author Manuscript

NIH-PA Author Manuscript

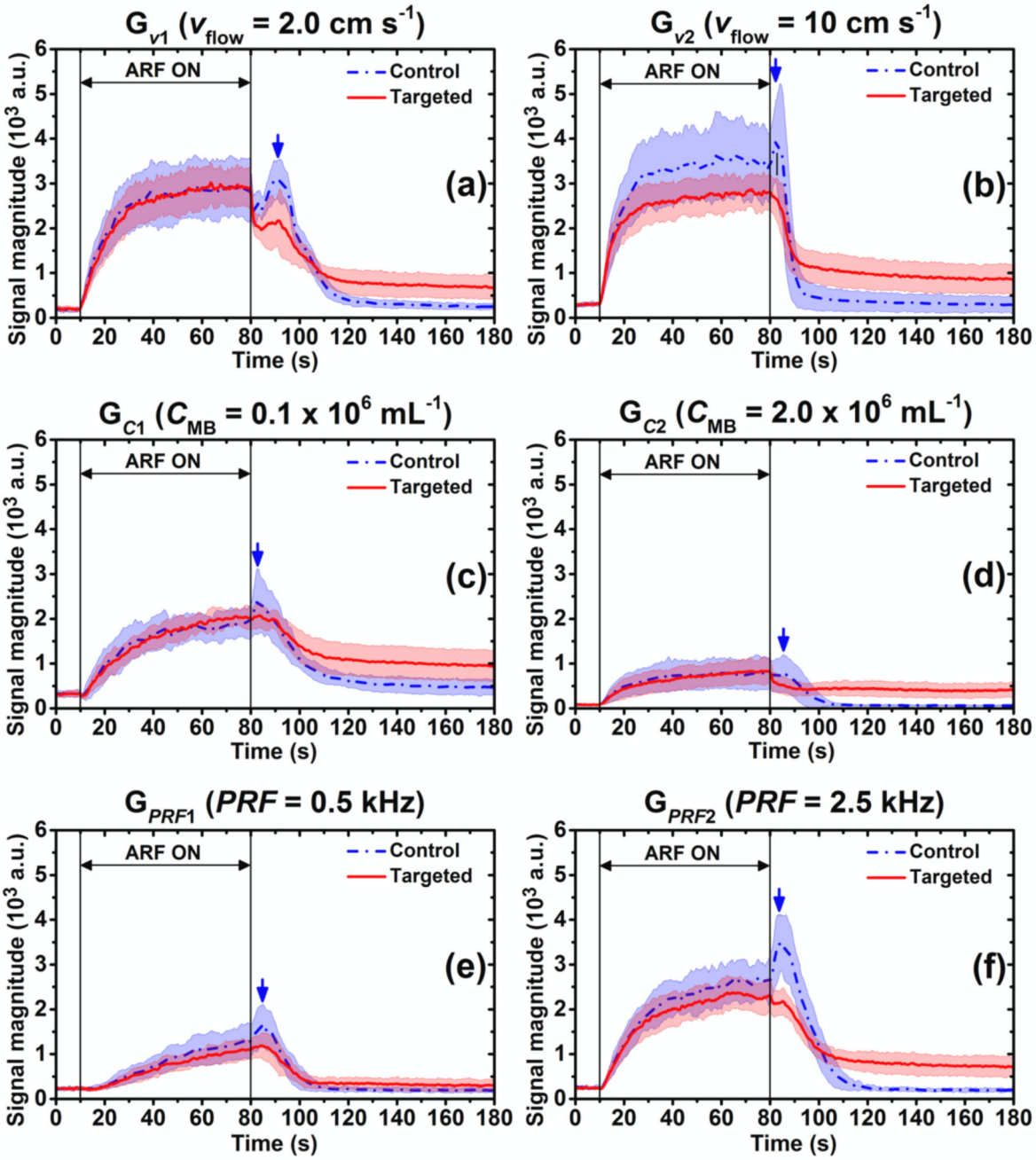

Figure 5.

Averaged signal magnitude curves of control (blue) and targeted (red) channels at different acoustic and flow conditions (table 2). (a) G_{v1} (v_{flow} = 2.0 cm s^{-1}) (b) G_{v2} (v_{flow} = 10 cm s^{-1}) (c) G_{C1} (*C*MB = 0.1 × 10^6 mL^{-1}) (d) G_{C2} (*C*MB = 2.0 × 106 mL^{-1}) (e) G_{PRF1} (*PRF* = 0.5 kHz) (f) G_{PRF1} (*PRF* = 2.5 kHz) Blue dash-dot and red solid lines indicate the mean values from 10 trials. Light color shadows indicate the corresponding error bars at the range of [mean ± standard deviation]. Blue arrows show the peaks of signal magnitude curves of

control channel at different groups: G_{v1}, t = 90.75 s; G_{v2}, t = 82.50 s; G_{C1}, t = 83.00 s; G_{C2}, t = 85.50 s; G_{PRF1}, t = 85.00 s; G_{PRF2}, t = 84.50 s.

NIH-PA Author Manuscript
NIH-PA Author Manuscript
NIH-PA Author Manuscript

NIH-PA Author Manuscript

NIH-PA Author Manuscript

NIH-PA Author Manuscript

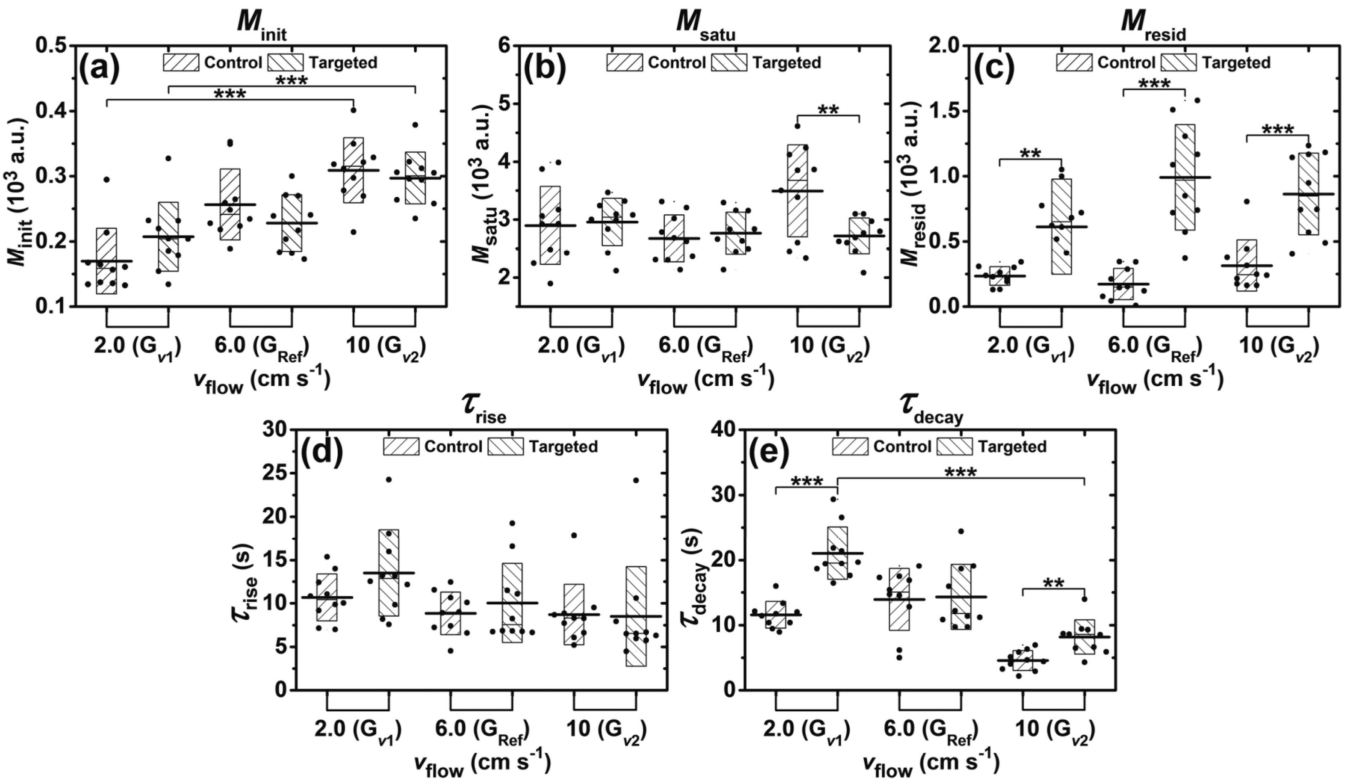

Figure 6.

Effects of flow velocities on parameters extracted from signal magnitude curves during modulated ARF experiments. Bar charts show the parameters of (a) M_{init}, (b) M_{satu}, (c) M_{resid}, (d) τ_{rise}, and (e) τ_{decay} averaged from 10 trials at different flow velocities and fluid channels. Boxes show the range of [mean ± standard deviation]. Black lines located at the center of the boxes show the corresponding mean value. Raw data from 10 trials are shown as solid dots overlaying the corresponding boxes. For Student's *t*-test, *: $p < 0.05$, **: $p < 0.01$, ***: $p < 0.001$, n = 10.

NIH-PA Author Manuscript

NIH-PA Author Manuscript

NIH-PA Author Manuscript

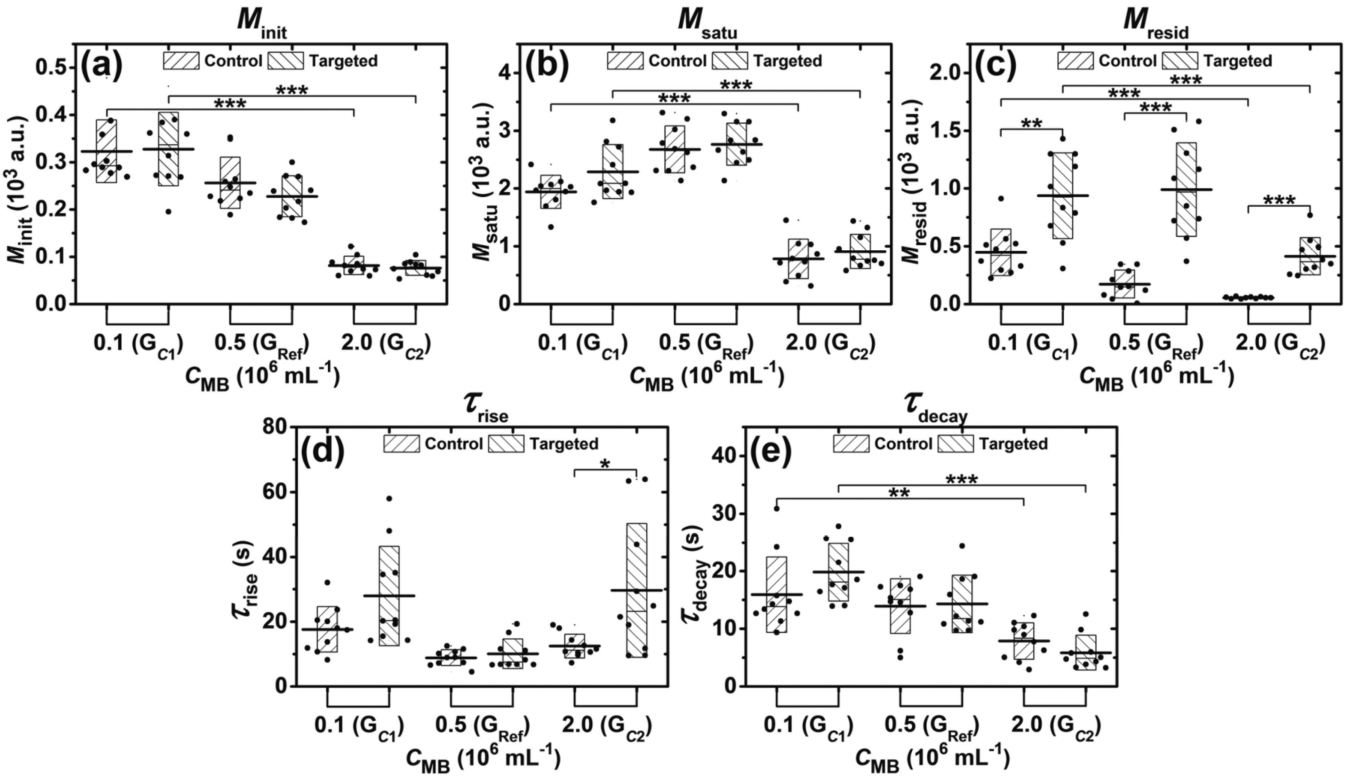

Figure 7.

Effects of microbubble concentration on parameters extracted from signal magnitude curves during modulated ARF experiments. Bar charts show the parameters (a) M_{init}, (b) M_{satu}, (c) M_{resid}, (d) τ_{rise}, and (e) τ_{decay} averaged from 10 trials at different microbubble concentration. Boxes show the range [mean ± standard deviation]. Black lines located at the center of the boxes show the corresponding mean value. Raw data from 10 trials are shown as solid dots overlaying the corresponding boxes. For Student's *t*-test, *: $p < 0.05$, **: $p < 0.01$, ***: $p < 0.001$, n = 10.

NIH-PA Author Manuscript

NIH-PA Author Manuscript

NIH-PA Author Manuscript

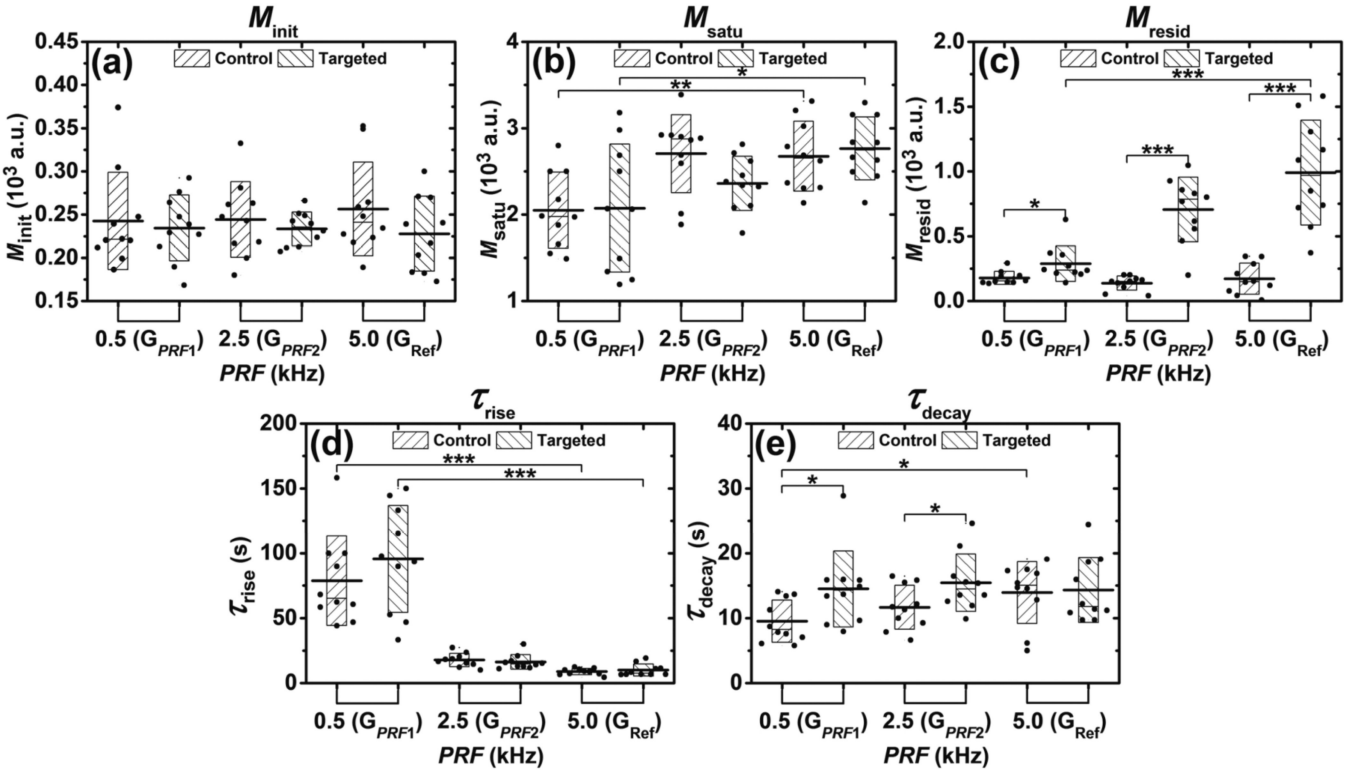

Figure 8.

Effects of ARF on parameters extracted from signal magnitude curves during modulated ARF experiments. Bar charts show the parameters (A) M_{init}, (B) M_{satu}, (C) M_{resid}, (D) τ_{rise}, and (E) τ_{decay} averaged from 10 trials at different *PRF* and fluid channels. Boxes show the range [mean ± standard deviation]. Black lines located at the center of the boxes show the corresponding mean value. Raw data from 10 trials are shown as solid dots overlaying the corresponding boxes. For Student's *t*-test, *: $p < 0.05$, **: $p < 0.01$, ***: $p < 0.001$, n = 10.

NIH-PA Author Manuscript

NIH-PA Author Manuscript

NIH-PA Author Manuscript

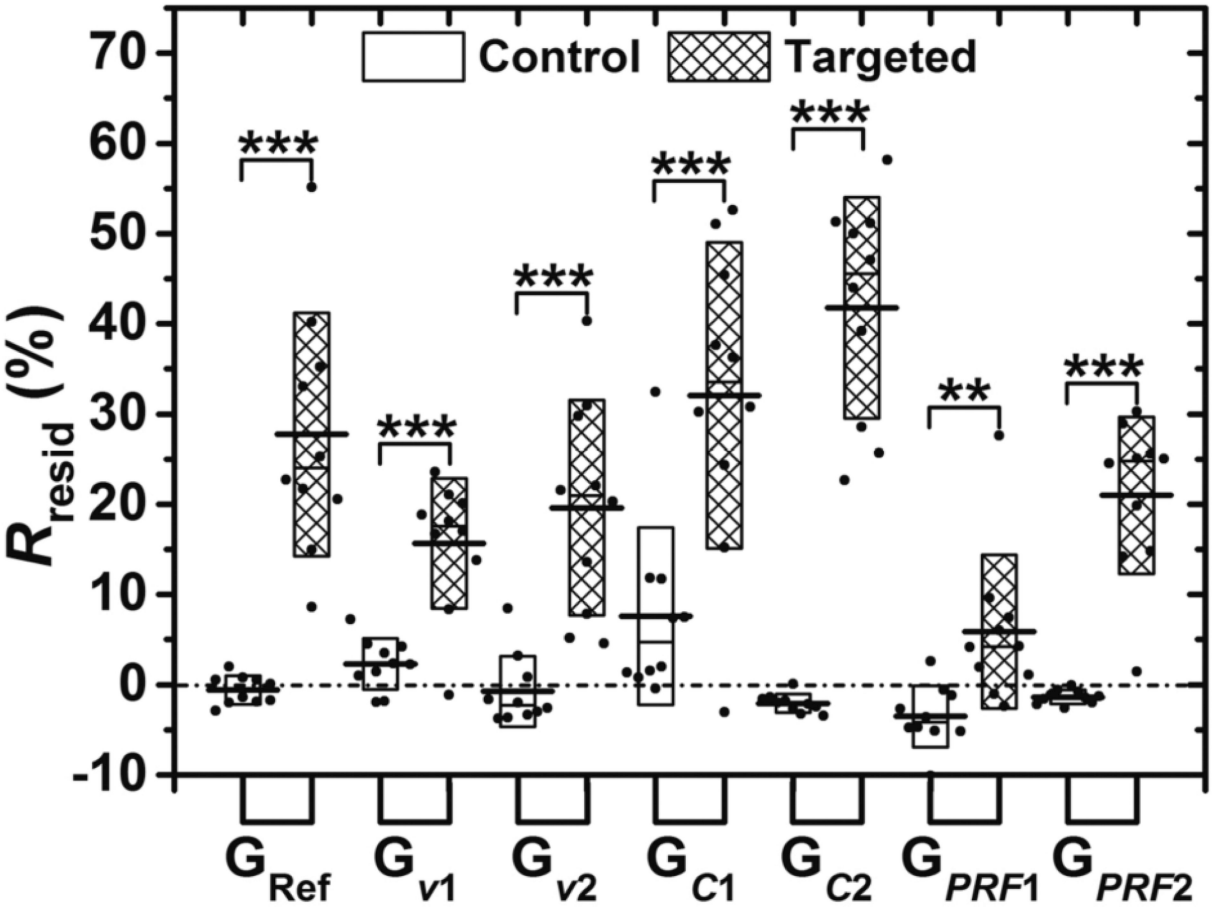

Figure 9.

The R_{resid} parameter across the various imaging conditions tested in this study. Boxes (empty for control channel and filled for targeted channel) show the range of [mean ± standard deviation]. Black lines located at the center of the boxes show the corresponding mean value. Raw data from 10 trials are shown as solid dots overlaid with corresponding boxes. For Student's *t*-test, **: $p < 0.01$, ***: $p < 0.001$, n = 10.

NIH-PA Author Manuscript

NIH-PA Author Manuscript

NIH-PA Author Manuscript

Table 1

Acoustic parameters used in various experiments

Pulse type	Imaging pulse	ARF pulse
Detail	Plane wave	Plane wave
	Center frequency = 4.5 MHz	Center frequency = 4.5 MHz
	Pulse length = 1 cycle	Pulse length = 15 cycles
	PRF[a] = 12 Hz	*PRF* = 0.5, 2.5, 5 kHz
	Peak-negative pressure = 12.3 kPa	Peak-negative pressure = 110.3 kPa
	MI[b] = 0.006	MI = 0.05
	Frame rate = 4 Hz[c]	

[a]Average pulse repetition frequency

[b]Mechanical index

[c]Echo data from three consecutive imaging pulses was used to form one image. Frame rate = *PRF* / 3 = 4 Hz.

NIH-PA Author Manuscript
NIH-PA Author Manuscript
NIH-PA Author Manuscript

Table 2

Flow and acoustic parameters for different groups of experiments

Parameter	Group name						
	G_{Ref}	G_{v1}	G_{v2}	G_{C1}	G_{C2}	G_{PRF1}	G_{PRF2}
v_{flow}[a] (cm s^{-1})	6.0	2.0	10	6.0	6.0	6.0	6.0
C_{MB}[b] (10^6 mL^{-1})	0.5	0.5	0.5	0.1	2.0	0.5	0.5
PRF (kHz)	5.0	5.0	5.0	5.0	5.0	0.5	2.5

[a] Flow velocity

[b] Microbubble concentration

NIH-PA Author Manuscript

NIH-PA Author Manuscript

NIH-PA Author Manuscript

Table 3

Effects of flow and acoustic conditions

Parameter	Variable		
	v_{flow} (figure 6)	C_{MB} (figure 7)	*PRF* (figure 8)
M_{init}	+[a]	−[b]	=[c]
M_{satu}	=	Not monotonic	+
M_{resid}	=	Control: − Targeted: not monotonic	Control: = Targeted: +
τ_{rise}	=	=	−
τ_{decay}	Control: not monotonic Targeted: −	−	Control: + Targeted: =

[a] Parameter increased with incremental increase in variable

[b] Parameter decreased with incremental increase in variable

[c] Parameter was unchanged with incremental increase in variable